



Development of a pilot-scale HuskyJet binder jet 3D printer for additive manufacturing of pharmaceutical tablets

Shing-Yun Chang^{a,b}, Jun Jin^c, Jun Yan^c, Xin Dong^d, Bodhisattwa Chaudhuri^{a,d},
Karthik Nagapudi^e, Anson W.K. Ma^{a,b,*}

^a Department of Chemical and Biomolecular Engineering, University of Connecticut, Storrs, CT 06084, USA

^b Polymer Program, Institute of Materials Science, University of Connecticut, Storrs, CT 06084, USA

^c Department of Statistics, University of Connecticut, Storrs, CT 06084, USA

^d Department of Pharmaceutical Sciences, University of Connecticut, Storrs, CT 06084, USA

^e Genentech, Inc, 465 East Grand Avenue, South San Francisco, CA 94080, USA

ARTICLE INFO

Keywords:

Binder jetting
Inkjet
Pharmaceutical tablets
Pilot-scale
Powder
Printer development

ABSTRACT

This paper reports a custom-built binder jet 3D printer for pilot-scale manufacturing of pharmaceutical tablets. The printer is equipped with high-throughput piezoelectric inkjet print heads and allows direct control of several key process parameters, including the build layer thickness, amount of jetted liquid binder, and powder spreading rate. The effects of these parameters on the properties of the as-printed tablets were studied using a powder mixture of lactose monohydrate and Kollidon® VA64 (KL) and an aqueous binder containing 5% of KL. The appropriate processing windows for two different powder spreading rates were identified, and the final properties of the printed samples were explained using a dimensionless “degree of overlap” parameter which is defined as the ratio between the penetrating depth of the binder into the powder and the build layer thickness. Lastly, 10% of indomethacin was added to the powder feedstock as a model drug. Drug-loaded tablets were produced at a rate of 32 tablets/min, having an average breaking force of 9.4 kgf, a friability of 2.5%, and an average disintegration time of 8 s. These properties are comparable to commercially available tablets and represent one of the best values reported in the literature of 3D printed tablets thus far.

1. Introduction

Additive manufacturing (AM) opens up a unique and exciting opportunity for mass customization. Regarding the use of AM for pharmaceutical applications, many papers and patents have documented concepts like controlling the drug dose and release profile for optimal therapeutic results and combining multiple prescription drugs in one tablet to improve medication adherence (Jamróz et al., 2018; Zema et al., 2017). AM also has the potential to disrupt the emerging practice of personalized medicine, in which the active pharmaceutical ingredients (API) and the corresponding dose are tailored to the patients' individual genetic profiles (Favier et al., 2014; Alomari et al., 2015). The drug release rate for a single or multiple APIs can be tailored through the choice of print materials and print designs (Infanger et al., 2019; Khaled et al., 2015; Goyanes et al., 2015). For instance, the incorporation of polymeric binders with a higher molecular weight and lower water solubility tends to produce printed tablets with a slower disintegration

rate (Katstra et al., 2000; Rowe et al., 2000). Likewise, tablets having a design with a lower surface-area-to-volume ratio tend to dissolve slower. Further, different drug release profiles can be engineered by varying the local material composition and/or creating multi-compartments through digital designs. To-date, a wide variety of release profiles, ranging from relatively simple profiles like sustained release (zero order) to more complex profiles such as multi-step and alternating pulse release, has been demonstrated (Haring et al., 2018; Khaled et al., 2015; Yu et al., 2009; Rowe et al., 2000). Solid dosage forms such as tablets and capsules have been successfully produced using many different AM methods, including fused deposition modeling (FDM) (Melocchi et al., 2020), semi-solid extrusion (Haring et al., 2018; Khaled et al., 2015), binder jet (Goole and Amighi, 2016), selective laser sintering (SLS) (Awad et al., 2019), and stereolithography (SLA) (Wang et al., 2016). Readers are encouraged to refer to several recent reviews on this topic (Souto et al., 2019; Jamróz et al., 2018; Zema et al., 2017).

Binder jet method has the advantage of room temperature operation,

* Corresponding author.

E-mail address: anson.ma@uconn.edu (A.W.K. Ma).

<https://doi.org/10.1016/j.ijpharm.2021.120791>

Received 16 April 2021; Received in revised form 2 June 2021; Accepted 6 June 2021

Available online 9 June 2021

0378-5173/© 2021 Elsevier B.V. All rights reserved.

which is suitable for APIs that are heat sensitive, compared to alternative methods such as FDM and SLS, in which the drug is subjected to high temperature. In binder jet 3D printing, solid powders are first spread onto a build plate, followed by the deposition of a liquid binder through an inkjet print head. Using a large array of small nozzles, binder jet is capable of creating finer patterns at a higher speed compared to a single nozzle approach such as semi-solid extrusion (Haring et al., 2018; Khaled et al., 2015). The loose powder also acts as a support material, making it possible to create overhang and more intricate structures. Compared to methods like FDM, SLS, semi-solid extrusion, 3D printed tablets produced by the binder jet method tend to have a higher porosity (typically on the order of 40–60%) (Meenashisundaram et al., 2020; Wilts et al., 2019; Infanger et al., 2019), which is desirable for fast dissolving applications and has been commercialized for treating epilepsy (FDA, 2015). However, the high porosity is also associated with a lower breaking force and high friability that severely limit binder jet as a more general platform technology for pharmaceutical manufacturing.

In this paper, we report the design, construction, and application of a pilot-scale binder jet 3D printer, named ‘HuskyJet’, for 3D printing pharmaceutical tablets containing a model small-molecule anti-inflammatory drug — indomethacin. Using the custom-built binder jet testbed, we explore how three key process parameters, namely, the build layer thickness, amount of jetted liquid binder, and powder spreading rate, affect the breaking force, friability, disintegration time, and shape fidelity of as-printed pharmaceutical tablets. The as-printed tablets in this study retain a fast disintegration rate, while possessing one of the highest breaking forces reported to date for 3D printed tablets.

2. Materials and methods

2.1. Powder materials and blending

Pharmaceutical-grade lactose monohydrate 310 NF (LM) used in this study was produced by Foremost and supplied by Kerry Inc. Indomethacin (Indo) powder from TCI Ltd. was used as a model API. The binder, Kollidon® VA64 (KL), was sourced from BASF Corp. All powders in the study were used as-received without further purification. In subsequent binder jet printing experiments, the KL binder was used in both the powder form and liquid form. In the powder form, KL was blended with LM and Indo. Blending of powders was carried out in a 16L stainless steel V-blender (Patterson Kelley Blendmaster Twin Shell Liquid/Solids Blender). The weighted powders were loaded to the stainless-steel shell and blended at 25 rpm for 18 min at room temperature with a maximum volume loading of 40%.

2.2. Binder liquid preparation

The liquid binder in this study contains 5% (w/v) KL in water. The inclusion of KL also increases the base viscosity of the binder and reduces the surface tension of water (Table S1), thereby suppressing satellite drop formation and stabilizing the jetting (Liu and Derby, 2019). To remove any undissolved or foreign particles that may clog the inkjet nozzles, the 5% KL solution was filtered through a 0.22- μ m polyethersulfone (PES) membrane (MilliporeSigma #GPWP04700). Further, to aid the visualization of the printed patterns on the powder bed, a small amount (0.4% by volume) of red liquid food dye (McCormick) was also added to the 5% KL solution through a syringe with a 0.45- μ m polyvinylidene difluoride (PVDF) filter (Whatman #6779-1304). The colored binder solution was then degassed by maintaining a low vacuum (30 in. Hg) for 1 h. Degassing reduces the chance of having bubbles in the liquid binder, which may lead to air locks within the print head geometry, thereby affecting jetting uniformity.

2.3. Custom-built HuskyJet binder jet 3D printer

Binder jetting experiments were performed using a custom-built

‘HuskyJet’ binder jet 3D printer (Fig. 1), equipped with three piezoelectric inkjet print heads (StarFire SG1024/MA, Dimatix, Fujifilm), a roller, and a moving sled that houses the feed and build platforms. The 3D printer was constructed by Integrity Industrial Inkjet Integration, Inc., USA. Each print head has 1,024 nozzles, arranged in eight rows. The ink jetting is actuated by sending an electrical waveform to the print head. Each nozzle row is individually programmable using graphical user interfaces (MetWave and MetPrint from Meteor Inkjet Ltd.). Tunable process parameters include the printhead temperature and waveform features such as actuation voltage, pulse width, and frequency. Each print head can be removed from the processing line and mounted directly onto a drop watcher system (JetXpert from ImageXpert Inc.) that allows the direct visualization of jetting behavior for different process parameters, which is an important feature for optimizing the jetting conditions and ink formulations. A single pulse waveform is used for drop imaging, and a sample image is shown in the inset figure of Fig. 3(a). The amount of liquid jetted per unit print area (mg/cm^2) was quantified by weighing the liquid dispensed from the print head and then normalizing the weight by the print area. The corresponding penetration depth of the binder into the powder bed was measured by recovering the consolidated layer after a single pass of liquid binder printing, followed by partial drying. The error bars represent the standard deviations based on measurements of five consolidated layers.

2.4. Binder jet printing experiments

In a typical print experiment, about 600 g of powder is first manually loaded into the feed platform of the moving sled and leveled by a stainless-steel dough scraper, as shown in schematic diagram (Fig. 2). A gap of ca. 400 μm is maintained between the roller and the top edge of the sled (Fig. 2a). To spread the powder, the build platform moves down by a set distance which corresponds to the build layer thickness while the feed platform moves up by two times the build layer thickness. The ratio between the increment of feed platform height and the corresponding decrement in build platform height defines the feed-to-powder ratio, or the amount of excessive powder fed from the feed platform to the build platform. The entire sled that houses both the feed and build platforms then passes under a rotating roller which pushes the powder from the feed platform to the build platform. The translational speed of the sled and the rotational speed of the roller are independently adjustable. Excess powder is collected by a spill tray that goes around the feed and build platforms. To prevent the printed object from sticking to the build platform, powder layers were spread to an initial thickness of 2-mm prior to dispensing the liquid binder for printing the actual object. The stand-off distance between the nozzle plate and the powder bed was set at 5 mm to prevent powder from unwantedly adhering to the nozzle plate due to powder splashing or electrostatics. The liquid binder solution is pre-loaded into the print head (via a recirculation reservoir) using a filter syringe (Fig. 1). The recirculation reservoir is optional in this study involving a soluble binder solution, but the recirculation feature is desirable for particle-laden inks that tend to settle by maintaining a constant fluid flow that helps resuspend any particulates. A slight negative pressure of 0.47 psi was applied to pull back the ink and prevent it from dripping through the nozzles. The as-printed samples were left to dry at room temperature overnight before being recovered from the powder bed for further characterization.

2.5. Experimental design: Process variables and outputs

Three key process parameters were varied in the experimental design of this study. They were the build layer thickness (l_b), the amount of jetted liquid per unit print area, namely the area density of binder liquid ($\bar{\rho}_{\text{liquid}}$), and the sled speed (v_{sled}) while the feed-to-powder ratio and roller speed were kept constant. Based on our previous formulation

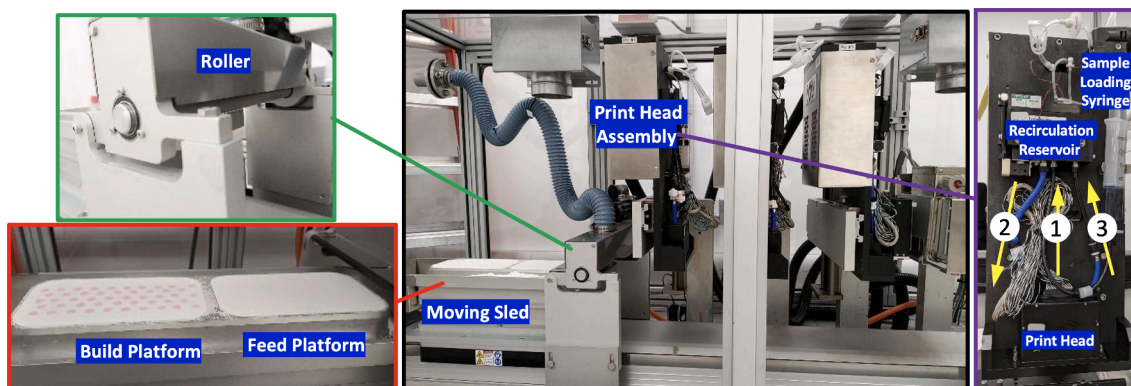


Fig. 1. Main components of the custom-built pilot-scale HuskyJet binder jet 3D printer. Each print head assembly consists of a recirculation reservoir and a print head (Dimatix SG 1024/MA). Arrows marked 1, 2, and 3 indicate the ink flow directions, namely from the loading syringe to the recirculation reservoir, from the recirculation reservoir to the print head, and from the print head back to the recirculation reservoir, respectively.

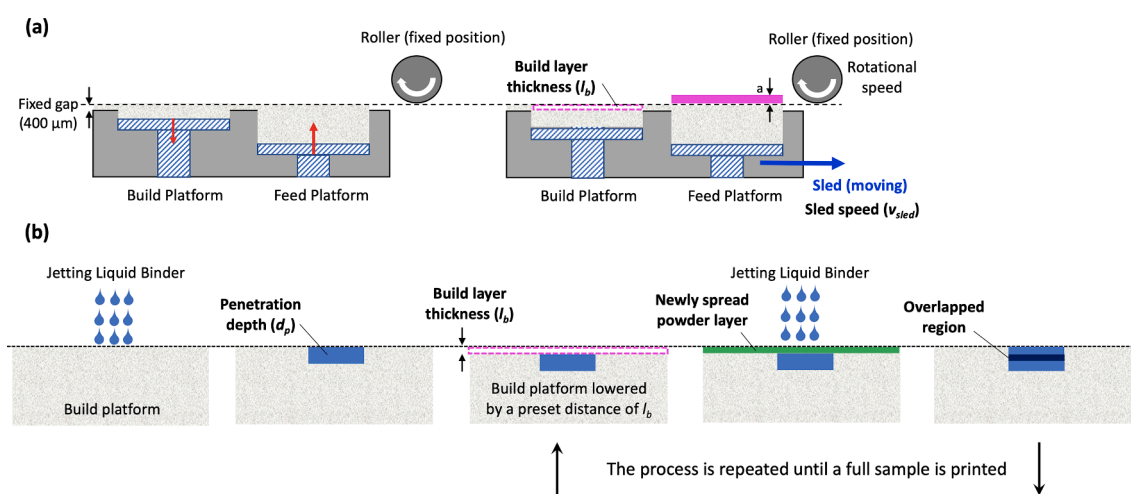


Fig. 2. A schematic diagram of the binder jet 3D printing process using the custom-built HuskyJet 3D printer. (a) Powder is spread by the roller from the feed platform to the build platform. The feed-to-powder ratio is defined as: a/l_b (b) shows the build platform as the liquid binder (blue color) is inkjet printed onto the powder bed. A newly spread powder layer is highlighted in green and the overlap between two printed (i.e., binder-wetted) layers is highlighted by a darker blue color. The process is repeated until the entire 3D object is completed.

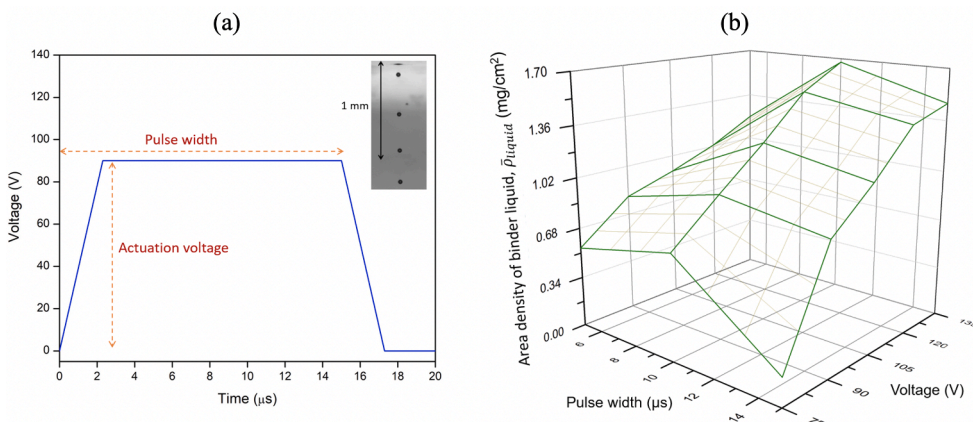


Fig. 3. (a) Jetting waveform for controlling the amount of liquid binder jetted through the piezoelectric print head. The inset figure shows the corresponding jetting image captured by the stroboscopic drop watching system. (b) Area density of binder liquid (ρ_{liquid}) jetted as a function of actuation voltage (V) and pulse width (μs). Print head set temperature: 25 °C.

Table 1
Controlled process parameters and dependent variables in this study.

Controlled Process Parameters	Values
Actuation voltage (V)	75, 105, 135
Pulse width (μs)	5, 10, 15
Meniscus pressure (psi)	0.47
Feed-to-powder ratio	2
Roller speed (rpm)	120
Layer thickness (l_b , μm)	100, 150, 250, 350
Sled speed (v_{sled} , mm/s)	100, 200
Dependent Variables	Descriptions
Area density of binder liquid ($\bar{\rho}_{liquid}$)	Depends on actuation voltage and pulse width for a given v_{sled}
Total amount of liquid per tablet (W_{liquid})	Depends on $\bar{\rho}_{liquid}$, l_b , and tablet volume
Penetration depth (d_p)	Depends on $\bar{\rho}_{liquid}$
Degree of Overlap (DO)	Depends on d_p and l_b

optimization study (Chang et al., 2020), a mixture of 90% (w/w) LM and 10% (w/w) KL was used as the powder feedstock and 5% (w/v) of KL in water was used as the liquid binder. The feed-to-powder ratio and roller rotational speed were fixed at 2 and 120 rpm, respectively. As previously mentioned, the build layer thickness is controlled by the decrement of the build platform height after each layer is printed. Drop watching experiments were performed for different actuation voltages (75 V, 105 V, and 135 V) and pulse widths (5 μs , 10 μs , and 15 μs) (Fig. S1). In subsequent binder jet printing experiments, the voltage was varied to change $\bar{\rho}_{liquid}$, while maintaining a constant pulse width of 10 μs . To produce round tablets with a diameter of 8.4 mm and a thickness of 5 mm, a filled-in circle with a diameter of 8.4 mm was printed repeatedly on the powder bed until a target thickness of 5 mm is reached. The number of repeats was calculated by dividing the total thickness of 5 mm by the selected build layer thickness and rounding up to the nearest integer. Two sled speeds, namely, 100 mm/s and 200 mm/s, were studied. In terms of output parameters, the breaking force, friability, disintegration times, bulk density, and shape of the printed tablets were recorded. The bulk density was calculated by dividing the mass of the tablet by the measured volume. Table 1 summarizes the controlled process parameters and key dependent variables in this study.

2.6. Characterization of printed tablets

The breaking force of printed tablets was measured on a hardness tester (HT300 Tablet Hardness Tester, Key International), compliant with the United States Pharmacopeia (USP) <1217> tablet breaking force protocol. Disintegration of the tablets was characterized using a tablet disintegration tester (Vanderkamp 10–911-71), which periodically submerges the test specimens into deionized water maintained at 37 °C and at a rate of 30 cycles/min, consistent with the USP <701> procedure. Finally, tablet friability was tested using a friability tester (TA Tablet Friability Tester, Erweka GmbH), operating at 25 rpm for 4 min at room temperature with a drop distance of 156 mm, following the USP <1216> method. Ten samples were measured to calculate the average breaking force and friability, and six samples were measured for disintegration time.

Indomethacin content in the printed tablets was determined using UV–Vis spectroscopy (Shimadzu UV-min) and was an average of three different tablets. To extract indomethacin, the printed tablets were first ground. 25–30 mg of the ground sample was then mixed with 10 mL ethanol using a stir bar for 2 hr in the dark to avoid photodegradation. The dispersion was then filtered through a 0.22- μm polytetrafluoroethylene (PTFE) filter and diluted tenfold. The absorbance of filtered solution at a wavelength of 319 nm was recorded. The calibration curve was generated by dissolving indomethacin in ethanol with a known concentration ranging from 10 to 50 $\mu\text{g}/\text{mL}$.

Particle size distribution of the dry powder was measured using a laser particle size analyzer (Malvern Mastersizer 2000). The distribution was described by D_{50} and D_{90} —50% and 90% of particles with a diameter below the stated diameter value, respectively. X-Ray Diffraction (XRD) was measured using a Bruker D2 PHASER 1D XRD instrument with a voltage of 30 kV and current of 10 mA. Scans were recorded using Cu K α radiation ($\lambda = 1.5418 \text{ \AA}$) for 2θ values ranging from 10 to 40° with a step size of 0.02° and an integration time of 0.5 s. XRD samples were prepared by completely dissolving the printed samples (with and without KL) in water, followed by drying at 45 °C and grinding.

2.7. Identifying processing windows with Support-Vector Machine (SVM)

Support-Vector Machine (SVM) is a supervised machine learning method for classification and regression analysis (Noble, 2006; Vapnik, 1995). For this application, the outcome variable is the quality of the printed tablets, a three-class categorical variable defined by the breaking force and shape of the printed tablets. The two predictors are the experiment factors, build layer thickness (l_b) and area density of binder liquid ($\bar{\rho}_{liquid}$). The processing windows for the two different sled speeds (v_{sled}) were obtained from SVM with Gaussian radial basis functions. Since the outcome variable is a multiclass variable, a multiclass SVM was used, where binary classifiers were built to distinguish every pair of

Table 2

Comparison between the custom-built HuskyJet Printer reported in this study and a commercial binder jet 3D printer (3D Systems CJP 660Pro) used in our previous study (Chang et al. 2020). The drying time is excluded from the printing rate calculations.

	ProJet CJP 660 Pro	HuskyJet
Print head type (number)	HP 11 (five)	Dimatix SG1024/MA (three)
Build volume	254 × 381 × 203 mm	140 × 100 × 40 mm
Print head type	Thermal	Piezoelectric
Nozzles per print head	304	1,024
Motion control	Gantry	Linear sled
Minimum powder amount required	15 kg	400–600 g
Printing rate (tablets/min)	1.3*	32**
Optional in-line curing (ultra-violet and infra-red)	No	Yes
Drop watcher	No	Yes

* Based on 40 tablets per batch. Build layer thickness: 100 μm ; default print head translational speed pre-set and cannot be changed by the user. **Based on 48 tablets per batch. Sled speed: 100 mm/s; build layer thickness: 100 μm ; sled travel distance of 1000 mm.

classes (one-versus-one) (Duan and Keerthi, 2005). LIBSVM with the Python interface was used in our application (Chang and Lin, 2011). For each SVM fit, the bandwidth of the Gaussian kernel and the regularity parameter were selected by the leaving-one-out cross-validation, which maximizes the area under the receiver operating characteristics curve over a grid of the two tuning parameters (Hastie et al., 2009).

Formal uncertainty measures for the classification boundary for the setting used are still lacking in the literature (Morais et al., 2019). To provide some uncertainty quantification, a nonparametric bootstrap approach (Efron, 1979) was used to resample the observed data 5000 times and an SVM was fitted to each bootstrap sample. For each bootstrap replicate, the bandwidth of the Gaussian kernel and the regularization parameter were kept the same as those selected for the original data. Overlaying the 5000 classification boundaries gives a visualization of the uncertainty for the inference about the target boundary.

3. Result and discussion

3.1. Special features of the HuskyJet printer

The HuskyJet printer is different from a commercial binder jet printer in a number of ways. Table 2 summarizes the key differences in specifications between the HuskyJet reported in this paper and a commercially available binder jet printer (3D Systems CJP 660Pro) used in our previous study (Chang et al., 2020). First, single-pass industrial print heads were chosen for HuskyJet to reduce the print time and increase the throughput. Tablets were produced at a rate of, at least, 32 tablets/min using the HuskyJet printer, compared to 1.3 tablets/min using the commercial printer. At this rate of 32 tablets/min, the HuskyJet printer has a similar throughput for powder filling machines like Xceladose which are routinely used for early phase clinical formulations. Second, the open architecture of the HuskyJet Printer allows the full control of various important process parameters for binder jet printing. For instance, the amount of binder is a key process parameter that

controls the binding effectiveness and consequently the mechanical properties of the printed objects. In our previous work that used a commercial turnkey printer (Chang et al., 2020), the binder amount dispensed via the built-in thermal jet print head could not be adjusted or optimized for different binders. The binder amount was controlled indirectly through the setting of “color saturation” in the user interface. The use of piezoelectric print heads of the HuskyJet 3D printer, in conjunction with the drop watcher system, further enables waveform optimization for jetting the liquid binder, which was impossible with the turnkey printer. The HuskyJet printer also allows the exploration of other key process parameters such as build layer thickness and powder spreading rate. Third, although a vibrational hopper may be integrated with the HuskyJet printer, the use of a two-elevator powder spreading mechanism significantly reduces the amount of powder required for performing proof-of-concept studies.

3.2. Controlling the amount of liquid binder via jetting waveforms

Based on previous formulation studies (Chang et al., 2020), 5% (w/v) KL in water was used as the liquid binder. The inclusion of KL, which is water-soluble, reduced the surface tension considerably from 72.0 to 46.9 mN/m while increasing the viscosity from 1 mPa s to 3.5 mPa s at 25 °C (Table S1). With a density of 1.01 g/cm³, the dimensionless viscosity, or Ohnesorge (*Oh*) number, was calculated to be ca. 0.1, which is on par with the recommended *Oh* value for inkjet fluids (Alamán et al., 2016). The actuation voltage and pulse width were varied (Fig. 3a), and the corresponding amount of liquid binder jetted for a single pass printing was measured and normalized by the print area, giving the area density of jetted binder liquid ($\bar{\rho}_{liquid}$). The results are summarized in Fig. 3b. $\bar{\rho}_{liquid}$ increased as a function of increasing voltage, consistent with previous studies (Liu and Derby, 2019). Three pulse widths (5, 10, and 15 μ s) were studied. For the same voltage, a pulse width of 10 μ s gave the highest $\bar{\rho}_{liquid}$. The non-monotonic dependence of $\bar{\rho}_{liquid}$ on pulse width may be explained by the superposition of newly generated

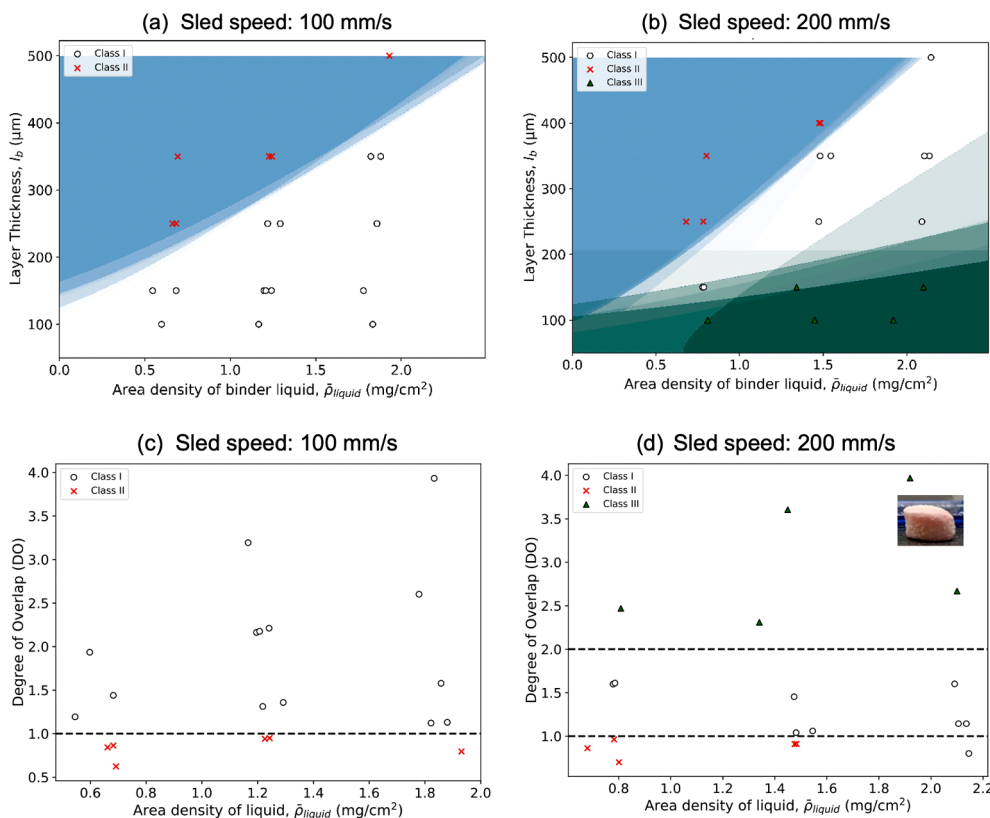


Fig. 4. Different classes of tablets produced using different build layer thicknesses (l_b) and area densities of binder liquid ($\bar{\rho}_{liquid}$) at a sled speed (v_{sled}) of: (a) 100 mm/s and (b) 200 mm/s. The boundaries are created using SVM with the Gaussian kernel. The bandwidth of the Gaussian kernel and the regularity parameter of the loss function were selected by leaving-one-out cross-validation for the area under the receiver operating characteristics curve. The uncertainty in the estimated boundaries represented by the changing darkness were obtained from 5000 bootstrap samples. (c) and (d) are the degree of overlap (DO) calculated as a function of $\bar{\rho}_{liquid}$ for $v_{sled} = 100$ mm/s and $v_{sled} = 200$ mm/s. Class I (>1 kgf; no shape distortion): unfilled circles; Class II (<1 kgf; no shape distortion): crosses; Class III (>1kgf; slanted). Dotted lines are added as visual aids.

pressure waves and reflected waves inside the print head, which further depends on the internal geometry of the print head and speed of sound traveling through the ink (Alamán et al., 2016). We hypothesize that at 10 μs , the newly generated pressure waves added to the reflected waves, thereby resulting in a higher pressure and consequently a larger amount of jetted liquid. To maximize the liquid binder to powder ratio, a pulse width of 10 μs was chosen. The amount of liquid binder jetted was varied by using a voltage of 75 V, 105 V and 135 V, respectively.

3.3. Establishing the processing windows using the degree of overlap between printed layers

Fig. 4a and b shows the processing windows as a function of build layer thickness (l_b) and area density of liquid binder jetted ($\bar{\rho}_{\text{liquid}}$). The smallest build layer thickness was chosen to be 100 μm — about two times larger than the median diameter (D_{50}) of the powder, which was measured to be 54 μm . Detailed particle size distribution data are included in Fig. S2. A $\bar{\rho}_{\text{liquid}}$ ranging from 0.5 to 2.1 mg/cm^2 was obtained by varying the actuation voltage of jetting waveform from 75 V to 135 V. Several printing experiments were repeated on multiple days, the $\bar{\rho}_{\text{liquid}}$ value was measured immediately before the printing experiment. A breaking force acceptance value of 1 kgf (=9.8 N) was chosen for establishing the initial processing window. Tablets with: (i) a breaking force exceeding 1 kgf and (ii) no shape distortion are classified as acceptable (Class I). Tablets having a breaking force less than 1 kgf are classified as Class II. At a lower sled speed of 100 mm/s (Fig. 4a), all the experimentally printed tablets belong to Class I or Class II. For a given l_b , a larger $\bar{\rho}_{\text{liquid}}$ tends to produce Class I tablets that are desirable. At a higher sled speed of 200 mm/s (Fig. 4b), a third regime (Class III) was observed. Within this regime, the printed tablets were slanted as shown, for example, in the inset figure. The decision boundaries between the

different classes were calculated based on SVM with the Gaussian kernel. The changing darkness at the boundaries shows the uncertainty in the boundary obtained from the bootstrap procedure.

These experimentally observed regimes can be understood in terms of the degree of overlap between the printed layers, as illustrated in Fig. 5. As the liquid binder is jetted onto the powder bed, the liquid both penetrates and spreads laterally within the powder bed. The drop penetration depth further depends on the total amount of liquid deposited (Miyajiri et al., 2018), wettability (Liu et al., 2017), and the pore structures (Mostafaei et al., 2020). A dimensionless Degree of Overlap (DO) between two sequentially printed layers may be defined as:

$$DO = \frac{d_p}{l_b} \quad (1)$$

where d_p is the penetration depth of the liquid binder and l_b is the build layer thickness.

To examine this hypothesis, the penetration depths (d_p) were measured for different $\bar{\rho}_{\text{liquid}}$ (Fig. 5b). The larger the $\bar{\rho}_{\text{liquid}}$, the larger d_p until a plateau is reached. For a fixed l_b , a larger $\bar{\rho}_{\text{liquid}}$ will result in a larger DO and more overlap between the printed layers. Some degree of overlap between printed layers is required to ensure good interlayer adhesion. Conversely, if DO is too small, the printed layer will not overlap, leading to delamination. The data in Fig. 4a and b are replotted using DO as the y-axis in Fig. 4c and d. The separation between Class I and Class II occurs at a DO value of ca. 1 for both sled speeds, supporting the hypothesis. For Class III, we hypothesize that the slanted tablets were a result of the higher shear associated with higher sled speed. Samples with a larger DO are more susceptible to shear-induced shape distortion as the total volume of the powder oversaturated with the liquid binder is likely to be larger, consistent with the study by Miyajiri

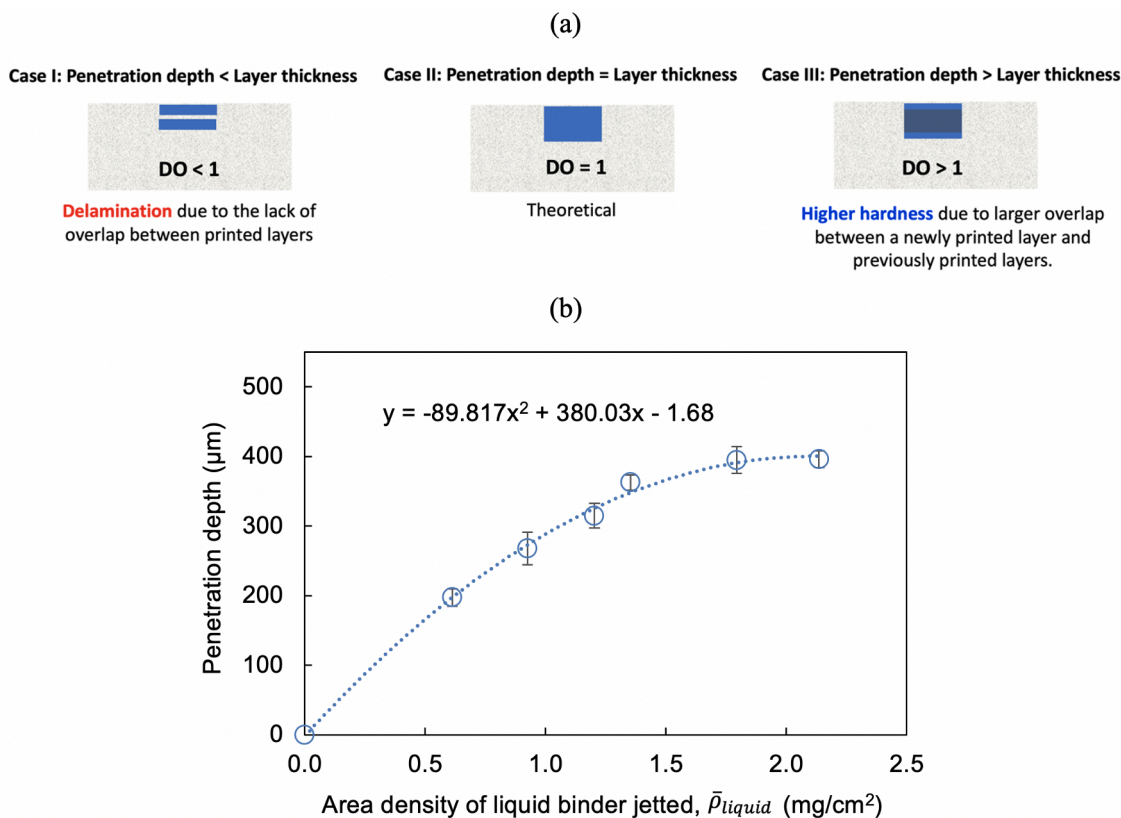


Fig. 5. (a) Illustration of printing with different degrees of overlap (DO) and the expected properties of the resulting printed samples. DO is calculated by dividing the measured penetration depth with the build layer thickness. For illustrative purposes, only two consecutively printed layers are shown. (b) Penetration depth as a function of area density of liquid binder jetted ($\bar{\rho}_{\text{liquid}}$). Liquid binder: 5% KL in water; Powder: 90% LM and 10% KL.

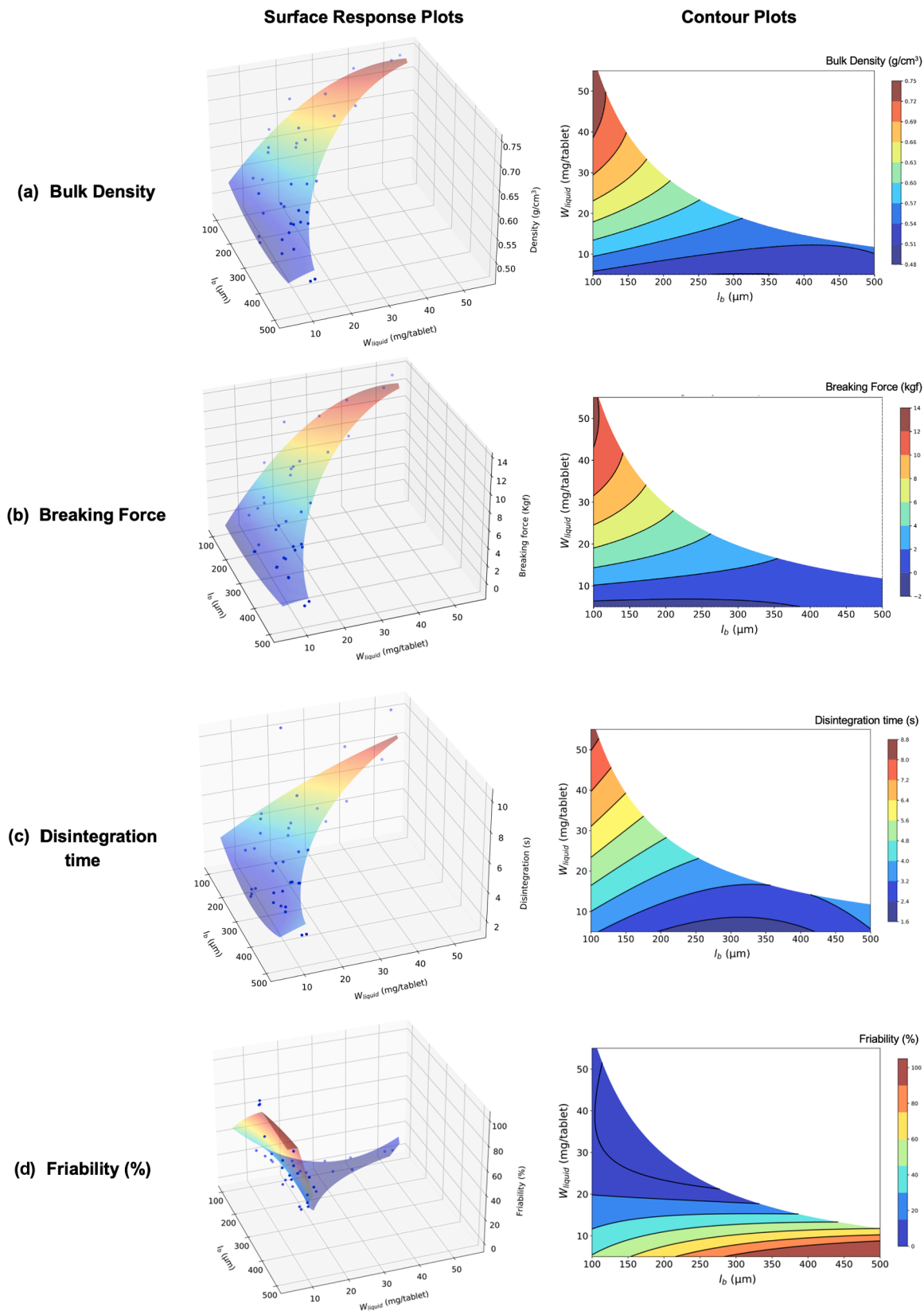


Fig. 6. Response surface plots and contour plots of: (a) density, (b) breaking force, (c) disintegration time, and (d) friability as a function of build layer thickness (l_b) and total liquid weight per tablet (W_{liquid}). Note on the contour plots, the upper right corners are experimentally inaccessible, as explained by Eq. (2). The response surface and contour plots are generated using Python with the *sklearn* package and a second-degree polynomial. For friability, any fitted values smaller than 0% or larger than 100% have been assigned as 0% and 100%, respectively.

et al. (2018). Experimentally, slanted tablets were observed above a DO value of 2 with a sled speed of 200 mm/s (Fig. 4d) while keeping all the remaining test conditions constant. In these experiments, the DO was independently varied for a fixed sled speed. In addition to sled speed and the degree of liquid binder oversaturation, the shear effects also likely depend on the size of the particles relative to the build layer thickness and the cohesiveness of the powder. At 200 mm/s, the onset of slanted tablets was observed as the build layer thickness approached the D_{90} of the print powder, which was measured to be 146 μm (Fig. S2).

3.4. Effects of key process parameters on printed tablet properties

Several key properties of the printed tablets were measured as a function of build layer thickness (l_b) and total amount of liquid per printed tablet (W_{liquid}). Response surface and contour plots for these properties as a function of l_b and W_{liquid} are shown in Fig. 6. It is worth noting that for a given build layer thickness (l_b), W_{liquid} was varied by adjusting the actuation voltage and consequently $\bar{\rho}_{liquid} \cdot W_{liquid}$ is related to l_b as:

$$W_{liquid} = \frac{\bar{\rho}_{liquid} \cdot A \cdot T_{tablet}}{l_b} = \frac{\bar{\rho}_{liquid} \cdot V_{tablet}}{l_b} \quad (2)$$

where A is the cross-sectional area of the tablet (0.55 cm^2) and T_{tablet} is the target thickness of the tablet (0.5 cm). Note that the number of printed layers per tablet is calculated by dividing T_{tablet} by l_b and then rounding up to the nearest integer, while the product of A and T_{tablet} gives the nominal volume (V_{tablet}) of a printed tablet (0.275 cm^3). Given that in this study all the tablets have the same target volume and the maximum value of $\bar{\rho}_{liquid}$ (per print head) is 2.1 mg/cm^2 as limited by the actuation voltage, there exists a maximum W_{liquid} for any given l_b . As a

result, the upper corner of the contour plot is inaccessible experimentally.

Nevertheless, the contour plots confirm that the density, breaking force, friability, and disintegration time depend on both process parameters, l_b and W_{liquid} . As W_{liquid} increases and l_b decreases, the bulk density of the printed tablets increases. This can be explained by the higher saturation level of the liquid binder within the powder as W_{liquid} increases and l_b decreases. Similar findings have been previously reported by a number of authors (Enneti and Prough, 2019; Vaezi and Chua, 2011). Printed tablets with a higher density tended to have a higher breaking force, lower friability, and longer disintegration time. This is consistent with a previous study by Lee et al. (2003). At least 11 mg of liquid binder per tablet (W_{liquid}) was required to achieve a breaking force above 1 kgf. Tablets with the highest breaking force of 12 kgf and no shape distortion was obtained using $l_b = 100 \mu\text{m}$, $W_{liquid} = 50.8 \text{ mg/tablet}$ (19% w/w), and $v_{sled} = 100 \text{ mm/s}$. This breaking force is considerably higher than our previous work using the same materials (Chang et al., 2020) and is comparable to pharmaceutical tablets that are currently available in the market (Quijano, 2018). Moreover, a breaking force of 12 kgf translates into a tensile strength of 1.8 MPa for the tablet which is generally accepted as a good value for ensuring the mechanical integrity of a tablet during production, storage and transportation. Further, no significant difference in appearance or breaking force was noted after the samples were stored for ten months in ambient lab environment (Table S2). A friability as low as 2% was obtained, close to the values reported in the recent previous studies (Infanger et al., 2019; Tian et al., 2019). The lower the friability, the less likely the printed tablets break during transportation. Although the friability value remains slightly higher than tablets produced using conventional tableting process, which is typically below 1% (Quijano, 2018), friability would not be a concern if the tablets are printed close to the point of use

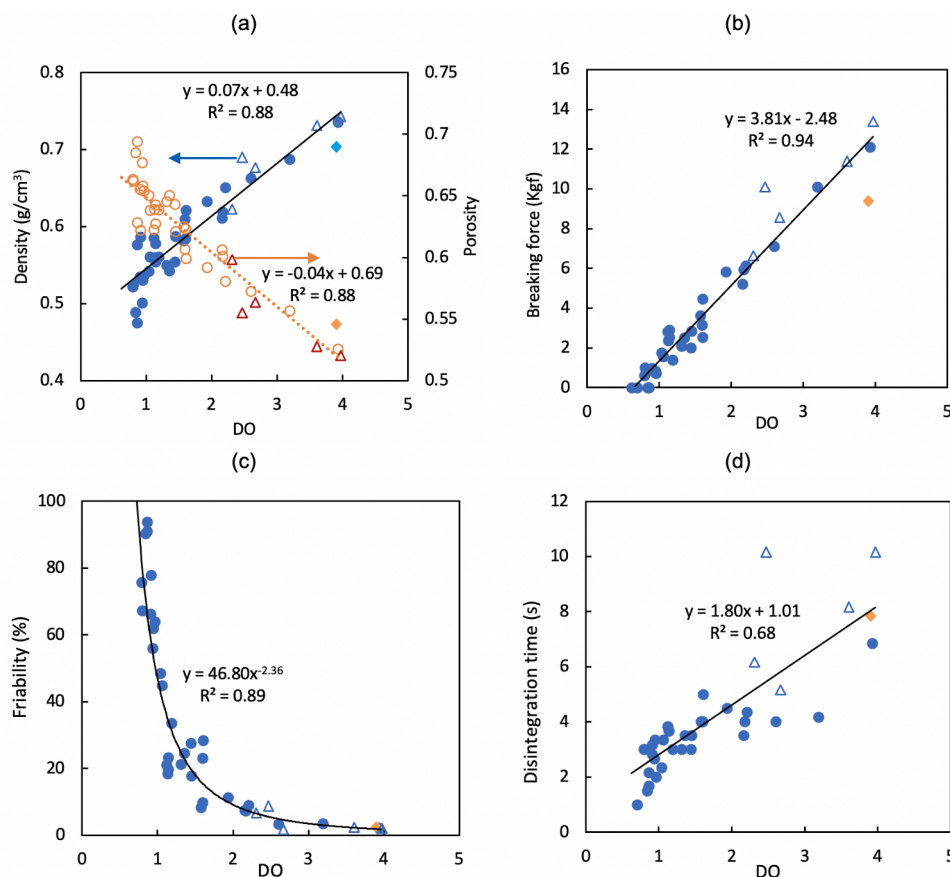


Fig. 7. (a) Bulk density and porosity, (b) breaking force, (c) friability, and (d) disintegration time of printed tablets as a function of degree of overlap (DO). Unfilled triangle: Slanted tablet; Diamond: tablet with API; Filled and unfilled circles: Non-deformed tablets. Porosity is calculated by $1 - \rho/\rho_p$, where ρ is the measured density of tablets and ρ_p is the LM particle density (1.55 g/cm^3) as reported by Kailay et al. (2011). Trendlines are added to guide the eyes and the equations shown are empirical fits based on experimental data in this study.

as a dispensing tool or as a research tool for quick formulation studies and clinical trials. Despite the relatively high breaking force, all the printed tablets disintegrated in less than 11 s, suitable for use as fast disintegrating tablets. For controlled-release applications, higher molecular weight components may be added to increase the disintegration time (Infanger et al., 2019), but this is beyond the scope of the current study.

Based on the concept of the degree of overlap of printed layers proposed in Fig. 5, various properties such as the bulk density, breaking force, friability and disintegration time were examined as a function of the dimensionless parameter, DO (Fig. 7). The experimentally measured density, breaking force, and disintegration time all show a linear correlation with DO, whereas friability follows a power-law dependence on DO. The measured density ranges from 0.47 to 0.74 g/cm³, whereas the porosity is inversely proportional to DO, ranging from 0.52 to 0.70. The corresponding empirical fits are included as equations in the figures. The larger discrepancy between the linear trend and the disintegration time data may be caused by the relatively large experimental error in measuring the relatively short disintegration time (<10 s) of the printed tablets. In these plots, circle symbols are used for tablets with no shape distortion, whereas data of slanted tablets are represented by triangles. Data of tablets containing the model API are included as diamonds. Further discussions on the inclusion of API are included in Section 3.6.

3.5. Effects of KL on LM crystallinity

The binder Kollidon VA64 (KL) in this study is a vinylpyrrolidone-vinyl acetate copolymer (PVP/VA), which has been specially formulated for use in granulation and as a dry binder. Many prior studies on binder jet printing of pharmaceutical tablets also use polyvinylpyrrolidone (PVP) as a binder. It has been hypothesized that PVP promotes binding strength because of the formation of hydrogen bonding with common excipients (Luo et al., 2021). However, the exact binding mechanism promoted by PVP is not entirely clear, especially for LM-based formulations. To address this question, tablets were printed with and without using KL in powder using the same processing conditions (the same l_b and v_{sled}) with water as the liquid binder. Tablets printed using 90% LM and 10% KL (solid) as powder feedstock have a breaking force of ca. 7.8 kgf and a disintegration time of 8 s (Table 3). In the absence of KL, the printed tablets showed a substantially lower average breaking force (1.68 kgf) and a longer average disintegration time (78 s) compared to the case with KL (Table 3). Given that LM is soluble in water, dissolution effect as the LM powder interacts with the aqueous binder must be considered. XRD was performed on the printed samples with and without KL to evaluate the crystallinity of LM in these samples. Specifically, the full width-half height maxima (FWHM) of major reflections from LM were compared (Kirk, 2007). Table 3 summarizes the XRD results and the 1D pattern is shown in Fig. S3. The

Table 3

Full width-half height maxima (FWHM) of the major reflections of α -lactose monohydrate XRD pattern, breaking force and disintegration time of tablets printed with 100% LM (100LM) and 90% LM and 10% KL (90LM10KL) using water as the liquid binder.

Angle (2 θ , °)	Full width-half height maxima (FWHM, °)	
	100LM	90LM10KL
12.6	0.16	0.25
16.5	0.15	0.27
19.3	0.29	0.33
19.7	0.19	0.31
20.1	0.19	0.33
21.0	0.18	0.41
21.4	0.20	0.35
Breaking force (kgf)	1.68 \pm 0.36	7.76 \pm 1.00
Disintegration time (s)	78 \pm 20	8 \pm 0

larger the FWHM, the lower the crystallinity. Tablets printed with KL consistently showed broader peaks compared to those without KL, suggesting the crystallinity is reduced in the presence of KL. This is consistent with the findings that PVP could reduce the crystallinity of spray-dried LM (Mahlin et al., 2006). The lower crystallinity of LM, or higher degree of amorphousness, may explain the higher breaking force as a result of stronger bonding, as suggested by Sebhathu and Alderborn, (1999). The lower crystallinity of LM due to KL would also explain the shorter disintegration time of the tablets containing KL.

3.6. Incorporation of indomethacin as a model active pharmaceutical ingredient

To directly compare the results of this study with our previous work using a commercial binder jet printer (Chang et al., 2020), a common nonsteroidal anti-inflammatory drug—indomethacin (Indo)—was chosen as a model active pharmaceutical ingredient (API). 10% of Indo was added to excipient powder containing 90% LM and 10% KL while keeping the ratio of LM to KL constant. The feedstock powder thus contains 81% LM, 9% KL, and 10% Indo. The tapped densities of the feedstock powders with and without Indo were measured to be 0.839 and 0.857 g/cm³, respectively. As in the case of excipient printing, 5% KL was used as the liquid binder. With the goal to increase the breaking force and reduce friability, the API-laden tablets were printed using a voltage of 135 V, a pulse width of 10 μ s, a sled speed of 100 mm/s, and a layer thickness of 100 μ m based on the best excipient printing results. The density, breaking force, friability, and disintegration time data of the printed tablets with and without the API are summarized in Table 4. The density of the API-laden tablets was measured to be 0.70 g/cm³ (porosity: 0.55), slightly lower than that of the excipient tablets at 0.74 g/cm³ (porosity: 0.52). The difference may be explained by the inclusion of Indo having a smaller average particle size (d_{50}) of 14 μ m, but also a long tail distribution of larger particles compared to the powder mixture of 90 %LM and 10% KL (Fig. S2). The lower breaking force and higher friability of the API-laden tablets are consistent with the lower density of the printed tablets whereas the disintegration time is comparable to the tablets without API. Additionally, we hypothesize that the poor water solubility and the lack of binding ability of Indo compared to KL may have negatively impacted the hydration and subsequent consolidation of the powder. The amount of Indo in the printed tablets was measured to be 9.6% \pm 0.3%, confirming the preservation of the API during the printing and subsequent drying. Fig. 8 compares the results of this study with existing literature on binder jet printing of pharmaceutical tablets. The as-printed tablets in this work possess a breaking force that is considerably higher than previous work and is comparable to commercial products, opening up the possibility of using this printing method as a more general platform technology for pharmaceutical manufacturing.

4. Conclusions

In this paper, we report the design and application of a custom-built

Table 4

Comparison between tablets with and without Indomethacin (Indo) printed using a voltage of 135 V, a pulse width of 10 μ s, a sled speed of 100 mm/s, and a layer thickness of 100 μ m. 90LM10KL: 90% LM and 10% KL. 81LM9KL10Indo: 81% LM, 9% KL, and 10% Indo.

Powder	90LM10KL	81LM9KL10Indo
Breaking force (kgf)	12.1 \pm 1.0	9.4 \pm 0.7
Friability (%)	2.2	2.5
Disintegration time (s)	7 \pm 1	8 \pm 1
Tablet weight (mg)	272	236
Diameter (mm)	9.12 \pm 0.12	8.88 \pm 0.08
Thickness (mm)	5.66 \pm 0.06	5.42 \pm 0.05
Density (g/cm ³)	0.74	0.70

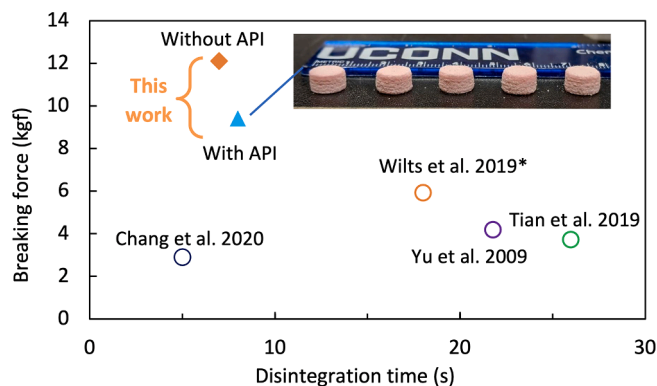


Fig. 8. Comparison of breaking force and disintegration time of 3D printed tablets in this study against prior work. Adapted from Chang et al. (2020). * Breaking force was calculated by multiplying the compressive strength reported by the cross-sectional area, assuming uniaxial compression. Inset figure shows five samples printed with a powder mixture containing 81% LM, 9% KL, and 10% Indo, using 5% KL in water as the liquid binder, a voltage of 135 V, a pulse width of 10 μ s, a sled speed of 100 mm/s, and a layer thickness of 100 μ m.

pilot-scale HuskyJet binder jet 3D printer for the additive manufacturing of pharmaceutical tablets. The printer is equipped with high-throughput piezoelectric print heads that further allow the control of jetting waveforms. Three key process parameters, namely, the build layer thickness, amount of liquid binder, and powder spreading rate, were varied. The effects of these parameters on the mechanical properties and shape fidelity of lactose-based tablets were studied. A dimensionless parameter called the Degree of Overlap (DO) between two printed layers is introduced to understand the processing windows and the final properties of the as-printed tablets. A small DO tends to produce tablets that are weak and prone to delamination due to the lack of overlap between the printed layers, whereas an exceedingly high DO, in combination with a fast powder spreading rate, has resulted in tablets with shear-induced shape distortions. For the lactose-based tablets studied in this work, a DO value between 1 and 2 produces tablets with good mechanical integrity and shape fidelity. Based on these results, a model active pharmaceutical ingredient (API) (Indomethacin) was added to the powder feedstock. The as-printed tablets possess one of the highest breaking forces, lowest friabilities, and highest throughputs reported in the literature of 3D printed tablets, while retaining fast disintegration, demonstrating the potential of using binder jet method as a more general manufacturing platform for the pharmaceutical industry. Furthermore, the HuskyJet printer is capable of producing tablets at a rate of 32 tablets/min making it amenable for use in early clinical studies and for proof-of-concept formulation experiments.

CRedit authorship contribution statement

Shing-Yun Chang: Conceptualization, Methodology, Investigation, Writing - original draft, Visualization. **Jun Jin:** Formal analysis, Writing - original draft, Visualization. **Jun Yan:** Formal analysis, Writing - review & editing, Supervision. **Xin Dong:** Investigation, Writing - review & editing. **Bodhisattwa Chaudhuri:** Resources, Writing - review & editing, Funding acquisition. **Karthik Nagapudi:** Resources, Writing - review & editing, Funding acquisition. **Anson W.K. Ma:** Conceptualization, Methodology, Writing - review & editing, Visualization, Supervision, Funding acquisition.

Declaration of Competing Interest

The authors declare that they have no known competing financial interests or personal relationships that could have appeared to influence the work reported in this paper.

Acknowledgements

The authors would like to acknowledge financial support from Genentech (USA), BASF Pharma Solutions (USA) and Kerry Inc. (USA) for providing in-kind materials for evaluation, and Anton Paar USA for instrument support. We also thank Dr. Robin Bogner for granting the research team access to the disintegration tester and Dr. Mingyang Tan for performing additional experiments to address reviewers' comments.

Appendix A. Supplementary material

Supplementary data to this article can be found online at <https://doi.org/10.1016/j.ijpharm.2021.120791>.

References

- Alamán, J., Alicante, R., Peña, J.I., Sánchez-Somolinos, C., 2016. Inkjet printing of functional materials for optical and photonic applications. *Materials* 9, 910. <https://doi.org/10.3390/ma9110910>.
- Alomari, M., Mohamed, F.H., Basit, A.W., Gaisford, S., 2015. Personalised dosing: Printing a dose of one's own medicine. *Int. J. Pharm.* 494, 568–577. <https://doi.org/10.1016/j.ijpharm.2014.12.006>.
- Awad, A., Fina, F., Trenfield, S.J., Patel, P., Goyanes, A., Gaisford, S., Basit, A.W., 2019. 3D printed pellets (Miniprintlets): A novel, multi-drug, controlled release platform technology. *Pharmaceutics* 11, 148. <https://doi.org/10.3390/pharmaceutics11040148>.
- Chang, C.C., Lin, C.J., 2011. LIBSVM: A Library for Support Vector Machines. *ACM Trans. Intell. Syst. Technol.* 2 <https://doi.org/10.1145/1961189.1961199>.
- Chang, S.Y., Li, S.W., Kowsari, K., Shetty, A., Sorrells, L., Sen, K., Nagapudi, K., Chaudhuri, B., Ma, A.W.K., 2020. Binder-jet 3D printing of indomethacin-laden pharmaceutical dosage forms. *J. Pharm. Sci.* 109, 3054–3063. <https://doi.org/10.1016/j.xphs.2020.06.027>.
- Duan, K.B., Keerthi, S.S., 2005. Which is the best multiclass SVM method? An empirical study. In: Oza, N.C., Polikar, R., Kittler, J., Roli, F. (Eds.), *Multiple Classifier Systems. MCS 2005. Lecture Notes in Computer Science*, vol. 3541. Springer, Berlin, Heidelberg. DOI: [10.1007/11494683_28](https://doi.org/10.1007/11494683_28).
- Efron, B., 1979. Bootstrap methods: Another look at the Jackknife. *Ann. Stat.* 7, 1–26. <https://doi.org/10.1214/aos/1176344552>.
- Enneti, R.K., Prough, K.C., 2019. Effect of binder saturation and powder layer thickness on the green strength of the binder jet 3D printing (BJ3DP) WC-12%Co powders. *Int. J. Refract. Met. Hard Mater.* 84, 104991 <https://doi.org/10.1016/j.ijrmhm.2019.104991>.
- Favier, J., Amar, L., Gimenez-Roqueplo, A.P., 2014. Paraganglioma and pheochromocytoma: From genetics to personalized medicine. *Nat. Rev. Endocrinol.* 11, 101–111. <https://doi.org/10.1038/nrendo.2014.188>.
- Goole, J., Amighi, K., 2016. 3D printing in pharmaceuticals: A new tool for designing customized drug delivery systems. *Int. J. Pharm.* 499, 376–394. <https://doi.org/10.1016/j.ijpharm.2015.12.071>.
- Goyanes, A., Martinez, P.R., Buanz, A., Basit, A.W., Gaisford, S., 2015. Effect of geometry on drug release from 3D printed tablets. *Int. J. Pharm.* 494, 657–663. <https://doi.org/10.1016/j.ijpharm.2015.04.069>.
- Haring, A.P., Tong, Y., Halper, J., Johnson, B.N., 2018. Programming of multicomponent temporal release profiles in 3D printed polytablets via core-shell, multilayer, and gradient concentration profiles. *Adv. Healthcare. Mater.* 7, 1800213. <https://doi.org/10.1002/adhm.201800213>.
- Hastie, T., Tibshirani, R., Friedman, J., 2009. *The Elements of Statistical Learning: Data Mining, Inference, and Prediction*, second ed. Springer, New York.
- Infanger, S., Haemmerli, A., Iliev, S., Baiar, A., Stoyanov, E., Quodbach, J., 2019. Powder bed 3D-printing of highly loaded drug delivery devices with hydroxypropyl cellulose as solid binder. *Int. J. Pharm.* 555, 198–206. <https://doi.org/10.1016/j.ijpharm.2018.11.048>.
- Jamroz, W., Szafraniec, J., Kurek, M., Jachowicz, R., 2018. 3D printing in pharmaceutical and medical applications – Recent achievements and challenges. *Pharm. Res.* 35, 176. <https://doi.org/10.1007/s11095-018-2454-x>.
- Kaialy, W., Martin, G.P., Ticehurst, M.D., Royall, P., Mohammad, M.A., Murphy, J., Nokhodchi, A., 2011. Characterisation and deposition studies of recrystallised lactose from binary mixtures of ethanol/butanol for improved drug delivery from dry powder inhalers. *AAPS J.* 13, 30–43. <https://doi.org/10.1208/s12248-010-9241-x>.
- Katstra, W.E., Palazzolo, R.D., Rowe, C.W., Giritlioglu, B., Teung, P., Cima, M.J., 2000. Oral dosage forms fabricated by Three Dimensional Printing. *J. Control. Release* 66, 1–9. [https://doi.org/10.1016/S0168-3659\(99\)00225-4](https://doi.org/10.1016/S0168-3659(99)00225-4).
- Khaled, S.A., Burley, J.C., Alexander, M.R., Yang, J., Roberts, C.J., 2015. 3D printing of tablets containing multiple drugs with defined release profiles. *Int. J. Pharm.* 494, 643–650. <https://doi.org/10.1016/j.ijpharm.2015.07.067>.
- Kirk, J.H., 2007. *Fundamental Structural Aspects of Crystalline Lactose Polymorphs*. Loughborough University.
- Lee, K.J., Kang, A., Delfino, J.J., West, T.G., Chetty, D., Monkhouse, D.C., Yoo, J., 2003. Evaluation of critical formulation factors in the development of a rapidly dispersing captopril oral dosage form. *Drug Dev. Ind. Pharm.* 29, 967–979. <https://doi.org/10.1081/DDC-120025454>.

- Liu, Y., Derby, B., 2019. Experimental study of the parameters for stable drop-on-demand inkjet performance. *Phys. Fluids* 31, 032004. <https://doi.org/10.1063/1.5085868>.
- Liu, Z., Wang, Y., Muzzio, F.J., Callegari, G., Drazer, G., 2017. Capillary drop penetration method to characterize the liquid wetting of powders. *Langmuir* 33, 56–65. <https://doi.org/10.1021/acs.langmuir.6b03589>.
- Luo, Y., Hong, Y., Shen, L., Wu, F., Lin, X., 2021. Multifunctional role of polyvinylpyrrolidone in pharmaceutical formulations. *AAPS PharmSciTech* 22, 34. <https://doi.org/10.1208/s12249-020-01909-4>.
- Mahlin, D., Berggren, J., Gelius, U., Engström, S., Alderborn, G., 2006. The influence of PVP incorporation on moisture-induced surface crystallization of amorphous spray-dried lactose particles. *Int. J. Pharm.* 321, 78–85. <https://doi.org/10.1016/j.ijpharm.2006.05.016>.
- Meenashisundaram, G.K., Xu, Z., Nai, M.L.S., Lu, S., Ten, J.S., Wei, J., 2020. Binder jetting additive manufacturing of high porosity 316L stainless steel metal foams. *Materials* 13, 3744. <https://doi.org/10.3390/ma13173744>.
- Melocchi, A., Uboldi, M., Parietti, F., Cerea, M., Foppoli, A., Palugan, L., Gazzaniga, A., Maroni, A., Zema, L., 2020. Lego-inspired capsular devices for the development of personalized dietary supplements: Proof of concept with multimodal release of caffeine. *J. Pharm. Sci.* 109, 1990–1999. <https://doi.org/10.1016/j.xphs.2020.02.013>.
- Miyajima, H., Orth, M., Akbar, J.M., Yang, L., 2018. Process development for green part printing using binder jetting additive manufacturing. *Front. Mech. Eng.* 13, 504–512. <https://doi.org/10.1007/s11465-018-0508-8>.
- Morais, C.L.M., Lima, K.M.G., Martin, F.L., 2019. Uncertainty estimation and misclassification probability for classification models based on discriminant analysis and support vector machines. *Anal. Chim. Acta* 1063, 40–46. <https://doi.org/10.1016/j.aca.2018.09.022>.
- Mostafaei, A., Elliott, A.M., Barnes, J.E., Li, F., Tan, W., Cramer, C.L., Nandwana, P., Chmielus, M., 2020. Binder jet 3D printing – Process parameters, materials, properties, and challenges. *Prog. Mater. Sci.* 100707 <https://doi.org/10.1016/j.pmatsci.2020.100707>.
- Noble, W.S., 2006. What is a support vector machine? *Nat. Biotechnol.* 24, 1565–1567. <https://doi.org/10.1038/nbt1206-1565>.
- Quijano, C.D., 2018. Directly Compressible ODT Platforms: A Comparative Study. Tablets & Capsules. CSC Publishing, Inc. MN.
- Rowe, C.W., Katstra, W.E., Palazzolo, R.D., Giritlioglu, B., Teung, P., Cima, M.J., 2000. Multimechanism oral dosage forms fabricated by three dimensional printing. *J. Control. Release* 66, 11–17. [https://doi.org/10.1016/S0168-3659\(99\)00224-2](https://doi.org/10.1016/S0168-3659(99)00224-2).
- Sebhatu, T., Alderborn, G., 1999. Relationships between the effective interparticulate contact area and the tensile strength of tablets of amorphous and crystalline lactose of varying particle size. *Eur. J. Pharm. Sci.* 8, 235–242. [https://doi.org/10.1016/S0928-0987\(99\)00025-1](https://doi.org/10.1016/S0928-0987(99)00025-1).
- Souto, E.B., Campos, J.C., Filho, S.C., Teixeira, M.C., Marins-Gomes, C., Zielinska, A., Carbone, C., Silva, A.M., 2019. 3D printing in the design of pharmaceutical dosage forms. *Pharm. Dev. Technol.* 24, 1044–1053. <https://doi.org/10.1080/10837450.2019.1630426>.
- Tian, P., Yang, F., Yu, L.P., Lin, M.M., Lin, W., Lin, Q.F., Lv, Z.F., Huang, S.Y., Chen, Y.Z., 2019. Applications of excipients in the field of 3D printed pharmaceuticals. *Drug Dev. Ind. Pharm.* 45, 905–913. <https://doi.org/10.1080/03639045.2019.1576723>.
- U.S. Food and Drug Administration and Research Center for Drug Evaluation, 2015. SPRITAM NDA 207958 Approval Package. https://www.accessdata.fda.gov/drugsatfda_docs/nda/2015/207958Orig1s000Approv.pdf.
- Vaezi, M., Chua, C.K., 2011. Effects of layer thickness and binder saturation level parameters on 3D printing process. *Int. J. Adv. Manuf. Technol.* 53, 275–284. <https://doi.org/10.1007/s00170-010-2821-1>.
- Vapnik, V.N., 1995. *The Nature of Statistical Learning Theory*. Springer, New York, 10.1007/978-1-4757-2440-0.
- Wang, J., Goyanes, A., Gaisford, S., Basit, A.W., 2016. Stereolithographic (SLA) 3D printing of oral modified-release dosage forms. *Int. J. Pharm.* 503, 207–212. <https://doi.org/10.1016/j.ijpharm.2016.03.016>.
- Wilts, E.M., Ma, D., Bai, Y., Williams, C.B., Long, T.E., 2019. Comparison of linear and 4-Arm star poly(vinyl pyrrolidone) for aqueous binder jetting additive manufacturing of personalized dosage tablets. *ACS Appl. Mater. Interfaces* 11, 23938–23947. <https://doi.org/10.1021/acsami.9b08116>.
- Yu, D.G., Branford-White, C., Yang, Y.C., Zhu, L.M., Welbeck, E.W., Yang, X.L., 2009. A novel fast disintegrating tablet fabricated by three-dimensional printing. *Drug Dev. Ind. Pharm.* 35, 1530–1536. <https://doi.org/10.3109/03639040903059359>.
- Zema, L., Melocchi, A., Maroni, A., Gazzaniga, A., 2017. Three-Dimensional Printing of Medicinal Products and the Challenge of Personalized Therapy. *J. Pharm. Sci.* 106, 1697–1705. <https://doi.org/10.1016/j.xphs.2017.03.021>.